Spin-Based Mach-Zehnder Interferometry in Topological Insulator p-n Junctions

Roni Ilan, Fernando de Juan, and Joel E. Moore

Spin-based Mach-Zehnder interferometry in topological insulator p-n junctions

Roni Ilan,[1, *] Fernando de Juan,[1, 2] and Joel E. Moore[1, 2]

[1] *Department of Physics, University of California, Berkeley, California 94720, USA*
[2] *Materials Sciences Division, Lawrence Berkeley National Laboratory, Berkeley, CA 94720*

Transport in three dimensional topological insulators relies on the existence of a spin-momentum locked surface state that encloses the insulating bulk. In this work we show how in a topological insulator p-n junction, a magnetic field turns this surface state into an electronic Mach-Zehnder interferometer. Transmission of the junction can tuned form zero to unity, resulting in virtually perfect visibility of the interference pattern, and the reflected and transmitted currents carry opposite spin polarization so that the junction also acts as a spin filter. Our setup therefore realizes a novel and highly tunable spintronic device where the effects of spin-momentum locking in TI surface states can be probed directly in a transport experiment.

Three dimensional topological insulators were discovered shortly after their prediction, by photoemission experiments demonstrating the existence of a single Dirac cone in their energy spectrum [1, 2]. In transport, the study of their properties has proved to be very challenging, mainly due to bulk carriers obscuring effects coming from the surface states, and limited control over chemical potentials. Recently, remarkable progress has been made both in growth of new types of topological insulator materials as well as measuring techniques: a new generation of compounds and alloys exhibit a low contribution to transport coming from bulk carriers, and improvements have been made in gating methods [3–6]. Hence, efforts can now be focused more on exploring exotic phenomena.

Dirac fermions confined to the surface of topological insulators are expected to exhibit remarkable effects: Chiral modes, topologically protected perfectly transmitting modes, as well as perfect Andreev reflection, are only some of the phenomena predicted to appear in transport [7–14]. In the presence of strong magnetic fields, Shubnikov de Haas oscillations and a quantum Hall effect typical to Dirac particles have already been demonstrated [15–21]. However, features unique to topological insulators such as the spin structure of the quantum Hall edge modes are yet to be observed. Here, we predict that a simple and rather common setup could pin-point these properties in the form of an interferometric measurement in a device made only from a film of TI, a top gate, and an external magnetic field. We show that a thin film of a topological insulator in the quantum Hall regime, partly covered by a gate, forms a p-n junction which in the presence of an in-plane flux functions as a condensed matter realization of a Mach-Zehnder interferometer. The oscillations in the conductance of this device are directly linked to the spin texture of the quantum Hall chiral modes, a manifestation of the spin-momentum locking property of TI surface states.

In addition to providing a testbed to reveal the unique transport properties of 3DTI, the structure we present here makes a spintronic device with a very high level of spin control. The two-path interferometer takes as inputs one dimensional currents that are naturally spin polar-ized without the aid of ferromagnetic leads, and generates as outputs two spin polarized channels that are spatially separated. The interference loop is controllable with the application of an in-plane flux, which determines how much spin current is carried in each output channel. In a two terminal geometry, the behavior of the conductance of this device is similar to that of the spin-FET, proposed by Datta and Das over two decades ago [22]. But our device functions more generally as a spin filter, granting separate access to the different spin orientations produced as outputs, and allowing to tune their relative amplitudes.

The idea of using a p-n junction to look for novel physical effects in Dirac materials traces back to the remarkable experiments done in graphene [23–25], where the interplay between Klein tunneling and the Quantum Hall Effect is responsible for characteristic transport signatures evidencing Dirac fermions [26, 27]. A p-n junction has also been studied theoretically before in TI [28], yet the effect we predict here was overlooked. When designing transport devices made out of a film of a 3DTI, a single flat surface is generally assumed for simplicity, while the effect described here requires considering the full 2D surface of a 3D bulk material. While superficially similar to "one quarter of" graphene, the surface state of TI is fundamentally different in that it lives on a closed surface with no edges, embedded in three dimensional space. The usual edge state picture of the Quantum Hall Effect is thus replaced by the more general principle that chiral modes appear between regions with different local Hall conductance. This is the main reason our design is unique to topological insulators and cannot be implemented in planar geometries.

Consider a thin film of a 3DTI in the presence of a strong perpendicular magnetic field, as shown in Fig. 1(a), so that the the top and the bottom surfaces are in the Quantum Hall regime with well developed Landau Levels. Since the surface state is a single Dirac fermion, when the $n = 0$ Landau Level is filled, the top surface has Hall conductance $\sigma_{xy} = 1/2$ in units of e^2/h. The bottom surface, penetrated by a magnetic field opposite in direction with respect to the surface normal, has $\sigma_{xy} = -1/2$
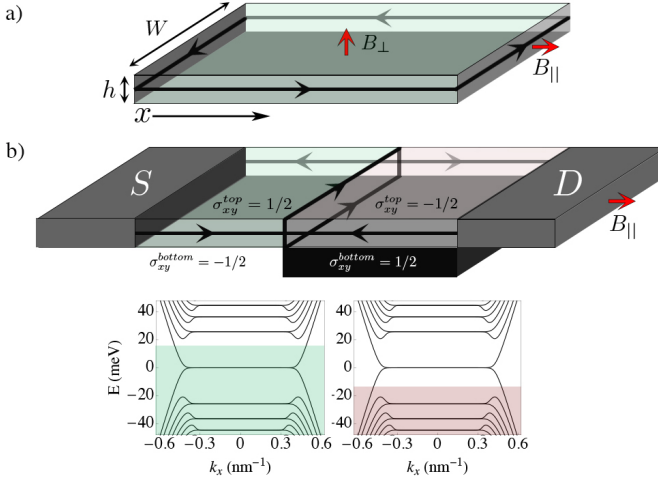
FIG. 1. a) A film of a 3DTI of height h and width W is placed under a strong perpendicular magnetic field $B_\perp$ and a parallel field $B_\parallel$. b) A 3DTI p-n junction in a magnetic field: a bottom gate shifts the chemical potential of the right side of the sample below the Dirac point, reversing σ_{xy} for the top and the bottom surfaces in this side. The film is then traversed by two additional chiral modes forming a closed loop around the bulk. The parallel field threads a flux ϕ through the loop. The energy spectrum of the surface states is plotted for an infinite film in the x direction, with $B_\perp = 2$ T, $h = 30$ nm, $W = 300$ nm. The green and red regions mark the chemical potential of the two sides of the junction. The gray boxes are contacts for the proposed two terminal measurement.

FIG. 2. Spin densities of the chiral modes of a 3DTI slab in a magnetic field, as a function of θ, a coordinate running along the circumference of the slab. Spin vectors are described in the tangent basis $\vec{s} = (s_x, s_\theta, s_\perp)$ which rotates along θ, keeping $s_\perp$ aligned with the surface normal.

[7]. This implies that the side surfaces, which are interfaces between regions where σ_{xy} changes by one unit, will carry a single chiral mode, similar to the one appearing in a quantum Hall state with $\sigma_{xy} = 1$ in a strictly 2D system.

To form a p-n junction, imagine gating half of the sample so that the chemical potential in the gated region resides between the $n = 0$ and $n = -1$ Landau levels. This flips the signs of the Hall conductances of the top and bottom surfaces, and as a result, the chirality of the current flowing on the side surfaces in the gated region is reversed. At the p-n junction, currents of opposite chirality meet at a vertex $v1$ on one side surface, and part from a vertex $v2$ on the other side. In addition, since the Hall conductance now changes sign not only from top to bottom, but also from right to left, two more chiral modes co-propagating along the junction connect v_1 and v_2, one running on the top and one on the bottom surface. Therefore, the p-n junction realizes a network of chiral modes with the structure of an interferometer, as shown in fig. Fig. 1(b). Crucially, because the modes traversing the film and forming the loop live in different surfaces, the loop encloses a finite area and an in-plane magnetic field can be used to thread flux through it, allowing the study of interference effects.
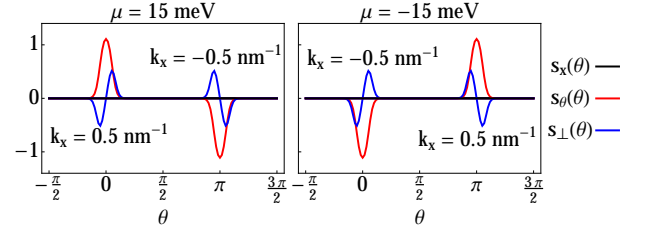
The key property of this network is that the chiral modes forming it have characteristic spin polarizations due to spin-momentum locking. To see this explicitly, we model our system as a Dirac fermion living on the surface of a rectangular slab placed in magnetic field [29], as in Fig. 1(a), and obtain the wave functions numerically. We then use these wave functions to calculated the expectation value of the different spin operators on the side surfaces, as well as the two terminal conductance across the p-n junction.

For the purpose of the numerical calculation, the surface is parametrized with two coordinates (x, θ), where x runs along the slab (perpendicular to the p-n junction) and $\theta \in [0, 2\pi]$ encircles the slab. Spin vectors are described using the basis $\vec{s} = (s_x, s_\theta, s_\perp)$ which rotates when moving along θ, keeping $s_\perp$ aligned with the surface normal. The Hamiltonian describing the Dirac fermion surface state of a 3DTI slab of height h and width W in a constant magnetic field is

$$H = -iv_F \hat{s}_\theta(\partial_x + ieA_x) + iv_F \hat{s}_x \frac{2\pi}{P}(\partial_\theta + i\frac{\phi}{2\pi}) - \mu \quad (1)$$

with P the perimeter $P = 2h + 2W$, v_F the Fermi velocity of the particles, μ the chemical potential, $\phi = 2\pi W h B_\parallel/(h/e)$ the flux trough the film cross section and $\hat{s}_i$ are the spin operators. The boundary conditions in the θ direction are anti-periodic [11]. In this coordinate system, the magnetic field is $\pm B_\perp$ for the top and bottom surfaces and zero for the sides, and is reproduced with a vector potential $A_x = A_x(\theta)$ as the one given in ref. [29]. The numerical diagonalization of this Hamiltonian is done by expanding the eigenfunctions in angular momentum states $\psi_k(s) = \sum_n e^{in\theta}\chi_{k,n}$ with n half-integer, as described in detail in ref. [29]. The energy spectrum obtained is shown in Fig. 1 for $B_\perp = 2$T, $h = 30$nm, $W = 300$nm. The spin polarization of the lowest Landau level side surface modes is obtained from the corresponding eigenstate $\psi_k(\theta)$ by calculating the expectation values $s_i(\theta) = \left\langle \psi_k^\dagger | \hat{s}_i | \psi_k \right\rangle$, and is shown on Fig. 3.

The expectation value of the different spin components is plotted as a function of θ in Fig. 3(b). As the fig-

ure shows, the average spin density on the side surfaces amounts to a net polarization perpendicular to the direction of the current flow. Changing the chirality of the current, either by flipping the direction of the field, or by changing the sign of the chemical potential, also reverses the direction of spin polarization. Hence, the chiral modes propagating along the side surfaces of the p-n junction carry opposite spin on opposite sides of the junction. Note that the effective spin always lies in the surface plane, and points from the region with $\sigma_{xy} = -1/2$ to the one with $\sigma_{xy} = 1/2$, and the same is correct for the modes traversing the junction.

The chiral modes traversing the sample on top and bottom surfaces have a different spin polarization than those at the side surfaces, and this is fundamental in generating interference effects in transport through the p-n junction. At the vertex $v1$, incoming modes have $\pm\theta$ polarization but outgoing modes have $\pm x$ polarization. Choosing specific spin operators for concreteness as $(\hat{s}_x, \hat{s}_\theta, \hat{s}_\perp) = (\sigma_x, \sigma_z, \sigma_y)$, an electron entering the vertex must be scattered into the outgoing modes according to the basis change

$$| \uparrow \rangle_z = \frac{1}{\sqrt{2}} | \uparrow \rangle_x + \frac{1}{\sqrt{2}} | \downarrow \rangle_x \qquad (2)$$

$$| \downarrow \rangle_z = \frac{1}{\sqrt{2}} | \uparrow \rangle_x - \frac{1}{\sqrt{2}} | \downarrow \rangle_x \qquad (3)$$

which means that the vertex $v1$ acts as a beam splitter. The same occurs at the vertex $v2$, with x and z interchanged. A schematic of this interferometer is shown in Fig. 3(c). Therefore, our setup has the exact structure of a two path interferometer, sketched in Fig. 3(d). The path of an electron emitted from a source contact at the left side splits into two paths at $v1$, propagating across the sample, and recombining at $v2$. Flux through the loop introduces a relative phase between the two arms of the interferometer. When this phase is zero, the electron recombines at v_2 with its spin orientation unchanged and is perfectly reflected, while a phase of π causes the incoming spin to be completely flipped so that perfect transmission occurs. Intermediate phases will result in an intermediate spin rotation and therefore, partial transmission. This spin-based interference effect can be directly observed in two-terminal transport.

To make our above statements quantitative, we compute the two terminal conductance across the p-n junction from the scattering matrix S of the device

$$S = \begin{pmatrix} r & t' \\ t & r' \end{pmatrix} \qquad (4)$$

with r, t, r', t' representing the reflection and transmission of incoming modes from a scattering region. The two terminal conductance from source to drain is simply calculated from the transmission matrix t and is given by
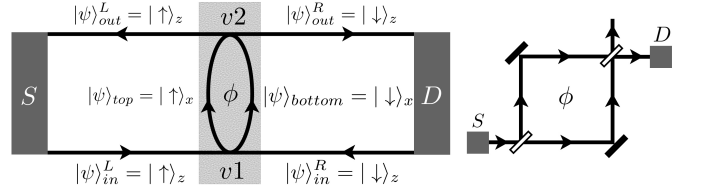
$$G = \frac{e^2}{h} |t|^2 \qquad (5)$$

FIG. 3. Left: A schematic of the interferometer and the effective spin states on each arm. The gray boxes on the sides are contacts, the light gray region in the middle is the scattering region: the vertices on the side surfaces labeled $v1, v2$ scatter the incoming spin states into rotated spin states on the top and bottom surfaces encircling the flux. Right: The original optical Mach Zehnder interferometer. The empty rectangles are the beam splitters, solid ones are fully reflecting mirrors.

Denoting the two incoming modes as $|\psi\rangle_{in}^L = | \uparrow \rangle_z$ and $|\psi\rangle_{in}^R = | \downarrow \rangle_z$ (see Fig. 3) the scattering matrix of the first vertex

$$S_{v1} = 1/\sqrt{2}(\sigma_x + \sigma_z) \qquad (6)$$

accounts for the scattering of the incoming modes onto $|\psi\rangle_{top}$ and $|\psi\rangle_{bottom}$, polarized along the x direction. The transfer matrix describing the propagation of the spinors $|\psi\rangle_{top}$ and $|\psi\rangle_{bottom}$ along the arms of the interferometer is diagonal, and contains two contributions. The first is a dynamical phase, e^{ikW}, where k is the momentum of the particles and W the width of the film. The second is a phase contributed by the flux enclosed in the loop, ϕ. It is therefore given by

$$T = e^{ikW + i\phi/2} e^{i\phi\sigma_z/2} \qquad (7)$$

Finally, from symmetry, the scattering matrix describing the second vertex v_2 is $S_{v2} = S_{v1}$. Therefore the total scattering matrix for the interference loop is the product of all three matrices

$$S = S_{v1} T S_{v2} = e^{ikW + i\phi/2} e^{i\phi\sigma_x/2} \qquad (8)$$

From this we find the simple expression

$$G = \frac{e^2}{h} \sin^2 \phi/2 \qquad (9)$$

As a function of flux through the loop, the conductance oscillates between zero and e^2/h.

We pause here to appreciate the fact that this interferometer has perfect visibility: the visibility of an interferometer is defined as $V = (I_{max} - I_{min})/(I_{max} + I_{min})$, where $I_{max(min)}$ are the maximum (minimum) of the current measured at the drain. Since the two beam splitters should split the current in half, we expect this interferometer to be very close to having unit visibility.

Equation (9) stems from the effective one dimensional model deduced from the spin densities we have calculated

numerically. In order to confirm the validity of this result, we perform an exact numerical calculation of the conductance of the p-n junction on the slab, again using the scattering matrix approach. A p-n junction is modeled by a chemical potential that changes sign at $x = 0$, $\mu(x) = \mu_L \theta(x) + \mu_R \theta(-x)$, with $\mu_L > 0$ and $\mu_R < 0$. The Hamiltonian is solved in the left and right sides with chemical potentials $\mu_L > 0$ and $\mu_R < 0$ respectively, and the wavefunctions are matched at the interface to obtain the transmission matrix, from which the conductance is calculated in a similar fashion to equation (5). As in ref. [29], this calculation involves both propagating and evanescent modes at the Fermi level [30, 31]. We define ψ_α^{L-} and ψ_α^{L+} with $\alpha = 1, \ldots, N_{\text{prop}}$ and $\psi_{\alpha'}^{L,ev}$ with $\alpha' = 1, \ldots, N_{\text{ev}}$ to be the incoming, outgoing, and evanescent modes at $x < 0$. Similarly, ψ_α^{R-}, ψ_α^{R+}, $\psi_{\alpha'}^{R,ev}$ are the corresponding modes at $x > 0$. The matching condition takes the form

$$\psi_\alpha^{L-} + \sum_{\beta=1}^{N_{\text{prop,L}}} r_{\alpha\beta} \psi_\beta^{L+} + \sum_{\alpha'=1}^{N_{\text{ev,L}}} c_{\alpha\alpha'} \psi_{\alpha'}^{L,ev} \qquad (10)$$

$$= \sum_{\beta=1}^{N_{\text{prop,R}}} t_{\alpha\beta} \psi_\beta^{R+} + \sum_{\alpha'=1}^{N_{\text{ev,R}}} c'_{\alpha\alpha'} \psi_{\alpha'}^{R,ev} \qquad (11)$$

where $r_{\alpha\beta}$ and $t_{\alpha\beta}$ are the elements of the reflection and transmission matrices from which the conductance can be calculated, $G = e^2/h \text{tr}(t^\dagger t)$.

Figure 4 shows the conductance as a function of flux through the loop and chemical potential or perpendicular field. As it shows, once Landau levels are well established and the two sides are brought into the lowest Landau level regime, the conductance oscillates with unit amplitude and a period of one flux quantum. This confirms the prediction of the effective model given by equation (9), and in particular the fact that the the interference pattern has unit visibility within the Dirac fermion model.

The range of chemical potentials where the system is in the lowest Landau level is determined by the height h and the magnetic length ℓ_B (see Ref.[33]), and for the parameters discussed is around $20 - 30$ meV, see Fig. 1. Beyond this range, additional chiral and non-chiral modes contribute to transport and the interference pattern is in general degraded (see figure 4 at a high chemical potential or low fields). h should also be kept larger than the threshold where the original Dirac fermions in top and bottom surfaces start to hybridize. In current samples setting $h > 10$ nm is sufficient [32]. We also note that deviation from unit visibility may be introduced due to hexagonal warping [34] and Zeeman coupling. The first becomes important at energies larger than $E^* \approx 230$ meV [34], and the second affects states only below the Zeeman energy, which at $B_\perp = 2$ T and g as large as 20 is only $E_Z = \mu_B g B_\perp/2 \approx 1.1$ meV. For the range of μ considered both effects can thus be safely neglected. For the same reason, a small offset of the chemical potential be-
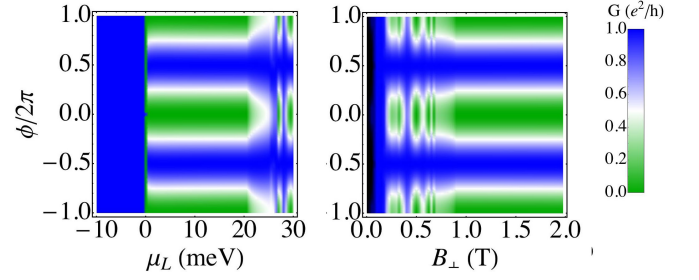

FIG. 4. Conductance of a p-n junction as a function of flux, chemical potential, and magnetic field. Left: Conductance as a function of ϕ and μ_L, for a fixed $\mu_R = -15$ meV and $B_\perp = 2$ T. Right: Conductance as a function of ϕ and $B_\perp$ for fixed $\mu_R = -\mu_L = 15$ meV. In both plots, once fully developed Landau levels are formed, and the chemical potential is in the lowest Landau level, the conductance follows equation (9).

tween top and bottom surfaces bears no consequence for this effect. Further corrections may arise from contact resistance in a two terminal measurement, multiplying the amplitude of oscillations by a non-universal factor. Such contributions could be eliminated, for example, by using multi-terminal setups. Lastly, the sample dimensions should not exceed the coherence length of chiral modes in 3DTI. While this quantity is currently unknown, it has been demonstrated in 2DEGs that it can reach ten of microns [35], so for the length scales described in this paper moderate disorder is not expected to affect our predictions. Coherent propagation may also be affected by thermal broadening of the momentum states, δk, which should satisfy $\delta k W \ll 1$, or $k_B T \ll v_F/W$. For the width we consider we find that the temperature should be kept lower than 1 K.

In summary, we have demonstrated that a p-n junction formed from a three dimensional topological insulator in the presence of a strong external perpendicular field and an in-plane flux can be turned into an interferometer which acts as a spin filter. The observation of conductance oscillations in this setup should serve as a clear-cut transport signature of spin momentum locking in 3DTI, and of the unusual spin texture of chiral modes in the quantum Hall regime. It is interesting to note the relation of our proposal with the electronic Mach-Zehnder interferometer realized in the beautiful experiment by Ji et al. [36] using Quantum Hall edge states in a two dimensional electron gas. There, the effect seen is purely charge-based and lacks the spin-filter aspect discussed here, which is unique to TI.

The oscillations in the two terminal conductance of our setup can also be thought of as an analog effect to the one appearing in the Datta-Das spin-FET [22]. There, the conductance between two ferromagnetic contacts can be changed by inducing a spin precession in the region that separates them through changing the spin-orbit coupling

with a gate voltage. In our setup, the input channels are naturally spin polarized so that normal contacts can be used rather than ferromagnetic leads, and the spin precession is induced by the in-plane flux. Compared to the spin-FET, our device has the outstanding advantage of spin-filtering, by physically separating the different spin components on output, which could be accessed using an appropriate contact configuration.

----

[*] rilan@berkeley.edu

[1] M. Z. Hasan and C. L. Kane, Rev. Mod. Phys. **82**, 3045 (2010).

[2] M. Z. Hasan and J. E. Moore, Annu. Rev. Condens. Matter Phys. **2**, 55 (2011).

[3] J. Zhang, C.-Z. Chang, Z. Zhang, J. Wen, X. Feng, K. Li, M. Liu, K. He, L. Wang, X. Chen, et al., Nat. Commun. **2**, 574 (2011).

[4] D. Kong, Y. Chen, J. J. Cha, Q. Zhang, J. G. Analytis, K. Lai, Z. Liu, S. S. Hong, K. J. Koski, S.-K. Mo, et al., Nat. Nanotech. **6**, 705 (2011).

[5] T. Arakane, T. Sato, S. Souma, K. Kosaka, K. Nakayama, M. Komatsu, T. Takahashi, Z. Ren, K. Segawa, and Y. Ando, Nat. Commun. **3**, 636 (2012).

[6] Y. Ando, J. Phys. Soc. Jpn. **82**, 102001 (2013).

[7] X.-L. Qi and S.-C. Zhang, Rev. Mod. Phys. **83**, 1057 (2011).

[8] D.-H. Lee, Phys. Rev. Lett. **103**, 196804 (2009).

[9] Y.-Y. Zhang, X.-R. Wang, and X. Xie, J. Phys.: Condens. Matter **24**, 015004 (2012).

[10] M. Sitte, A. Rosch, E. Altman, and L. Fritz, Phys. Rev. Lett. **108**, 126807 (2012).

[11] J. H. Bardarson and J. E. Moore, Rep. Prog. Phys. **76**, 056501 (2013).

[12] L. Fu and C. L. Kane, Phys. Rev. Lett. **100**, 096407 (2008).

[13] L. Fu and C. L. Kane, Phys. Rev. Lett. **102**, 216403 (2009).

[14] A. R. Akhmerov, J. Nilsson, and C. W. J. Beenakker, Phys. Rev. Lett. **102**, 216404 (2009).

[15] C. Brüne, C. X. Liu, E. G. Novik, E. M. Hankiewicz, H. Buhmann, Y. L. Chen, X. L. Qi, Z. X. Shen, S. C. Zhang, and L. W. Molenkamp, Phys. Rev. Lett. **106**, 126803 (2011).

[16] P. Cheng, C. Song, T. Zhang, Y. Zhang, Y. Wang, J.-F. Jia, J. Wang, Y. Wang, B.-F. Zhu, X. Chen, et al., Phys. Rev. Lett. **105**, 076801 (2010).

[17] D.-X. Qu, Y. Hor, J. Xiong, R. Cava, and N. Ong, Science **329**, 821 (2010).

[18] J. G. Analytis, R. D. McDonald, S. C. Riggs, J.-H. Chu, G. Boebinger, and I. R. Fisher, Nat. Phys. **6**, 960 (2010).

[19] D. Kozlov, Z. Kvon, E. Olshanetsky, N. Mikhailov, S. Dvoretsky, and D. Weiss, Phys. Rev. Lett. **112**, 196801 (2014).

[20] R. Yoshimi, A. Tsukazaki, Y. Kozuka, J. Falson, K. S. Takahashi, J. G. Checkelsky, N. Nagaosa, M. Kawasaki, and Y. Tokura, arXiv:1409.3326v1 (2014).

[21] Y. Xu, I. Miotkowski, C. Liu, J. Tian, H. Nam, N. Alidoust, J. Hu, C.-K. Shih, M. Zahid Hasan, and Y. P. Chen, ArXiv:1409.3778 (2014).

[22] S. Datta and B. Das, Applied Physics Letters **56**, 665 (1990).

[23] J. Williams, L. DiCarlo, and C. Marcus, Science **317**, 638 (2007).

[24] N. Stander, B. Huard, and D. Goldhaber-Gordon, Phys. Rev. Lett. **102**, 026807 (2009).

[25] A. F. Young and P. Kim, Nature Physics **5**, 222 (2009).

[26] D. Abanin and L. Levitov, Science **317**, 641 (2007).

[27] J. Tworzydło, I. Snyman, A. Akhmerov, and C. Beenakker, Phys. Rev. B **76**, 035411 (2007).

[28] J. Wang, X. Chen, B.-F. Zhu, and S.-C. Zhang, Phys. Rev. B **85**, 235131 (2012).

[29] F. de Juan, R. Ilan, and J. H. Bardarson, Phys. Rev. Lett. **113**, 107003 (2014).

[30] D. H. Lee and J. D. Joannopoulos, Phys. Rev. B **23**, 4988 (1981).

[31] A. Umerski, Phys. Rev. B **55**, 5266 (1997).

[32] Y. Zhang, K. He, C.-Z. Chang, C.-L. Song, L.-L. Wang, X. Chen, J.-F. Jia, Z. Fang, X. Dai, W.-Y. Shan, et al., Nature Physics **6**, 584 (2010).

[33] See supplementary material section.

[34] L. Fu, Phys. Rev. Lett. **103**, 266801 (2009).

[35] P. Roulleau, F. Portier, P. Roche, A. Cavanna, G. Faini, U. Gennser, and D. Mailly, Physical Review Letters **100**, 126802 (2008).

[36] Y. Ji, Y. Chung, D. Sprinzak, M. Heiblum, D. Mahalu, and H. Shtrikman, Nature **422**, 415 (2003).